Agricultural and Forest Meteorology 233 (2017) 183–194

Contents lists available at ScienceDirect

Agricultural and Forest Meteorology

journal homepage: www.elsevier.com/locate/agrformet

# Spatiotemporal change and trend analysis of potential evapotranspiration over the Loess Plateau of China during 2011–2100

Shouzhang Peng[a,b], Yongxia Ding[c], Zhongming Wen[a,b], Yunming Chen[a,b,*], Yang Cao[a,b], Jingyu Ren[d]

[a] State Key Laboratory of Soil Erosion and Dryland Farming on the Loess Plateau, Northwest A&F University, Yangling 712100, China
[b] Institute of Soil and Water Conservation, Chinese Academy of Sciences and Ministry of Water Resources, Yangling 712100, China
[c] College of Earth Environmental Sciences, Lanzhou University, Lanzhou 730000, China
[d] Institute of Soil and Water Conservation, Northwest A&F University, Yangling 712100, China

ARTICLE INFO

*Article history:*
Received 13 September 2016
Received in revised form
19 November 2016
Accepted 24 November 2016
Available online 30 November 2016

*Keywords:*
Potential evapotranspiration
Delta downscaling
Hargreaves model
Mann–Kendall trend test
Sen's slope estimator
Loess plateau

ABSTRACT

The spatiotemporal change and trend of annual potential evapotranspiration (PET) over the Loess Plateau of China from 2011 to 2100 are assessed in this work. PET is calculated using the Hargreaves model with monthly mean, maximum, and minimum temperatures and a 1 km spatial resolution, which are generated using the Delta downscaling method and general circulation models (GCMs) with four representative concentration pathway (RCP) scenarios. The PET trend is detected via Mann–Kendall and Sen's slope estimator tests. The following results are drawn: (1) the Delta downscaling method shows a favorable performance in detecting GCM monthly temperatures based on the mean absolute error and regression analysis between downscaled data and independent surface observations. Among the 28 GCMs, the NorESM1-M and GISS-E2-R models show the best performance in reproducing the monthly mean/maximum and minimum temperatures over the Loess Plateau, respectively; (2) the average annual PET over this region will increase by 12.7%–23.9% from 1961 to 1990 to the end of this century (2071–2100). However, these increments show strong spatial variations; (3) the annual PET during the 2011–2100 period at each grid of the region demonstrates a significantly increasing trend under each RCP scenario, while RCP2.6, RCP4.5, RCP6.0, and RCP8.5 have average magnitudes of trend of 10.4 mm/10yr, 17.7 mm/10yr, 21 mm/10yr, and 29.7 mm/10yr, respectively; (4) the annual PET with significant trends during the other three periods (2011–2040, 2041–2070, and 2071–2100) present various spatial distributions in their magnitudes of trend under the aforementioned RCP scenarios. RCP2.6 showed a significant decrease during 2041–2070 and 2071–2100, although such trends are only observed at 0.3% and 1.2% of the Loess Plateau, respectively; and (5) the spatial results provide some information, such as locations and area ratios, which are valuable in assessing future PET changes and trends. These spatiotemporal results represent the PET changes and trends in detail and provide insights for developing flexible adaptation and mitigation strategies to combat the effects of global warming in this region.



## 1. Introduction

The Loess Plateau (LP) of China is known for its severe soil erosion (Sun et al., 2015). Given that most areas in this region have semiarid and sub-humid climates with an annual mean precipitation (1961–2009) of 143.6 mm–811.8 mm along the southeast–northwest direction, the LP is also threatened by severe water shortage (Li et al., 2012a). Over the past 50 years, the annual precipitation and air temperature over the LP decreased and increased, respectively (Bi et al., 2009; Miao et al., 2011; Sun et al., 2015; Wang et al., 2012), thereby exacerbating the water shortage and threatening the development of this region (Li et al., 2012a). Under the effects of global warming, the temperature over the LP will continuously increase throughout the century (Li et al., 2012b) and subsequently accelerate the water loss in this region (Aouissi et al., 2016). Potential evapotranspiration (PET) is a key hydrological variable for quantifying water loss in a region; this variable can be used to calculate actual evapotranspiration, schedule irrigation projects, and prepare input data for hydrological models (Aouissi et al., 2016; Li et al., 2012a). Therefore, the future PET in the LP

* Corresponding author at: No. 26, Xinong Road, Institute of Soil and Water Conservation, Yangling, Shaanxi 712100, China.
*E-mail address:* ymchen@ms.iswc.ac.cn (Y. Chen).

http://dx.doi.org/10.1016/j.agrformet.2016.11.129
0168-1923/

must be investigated to develop suitable adaptation and mitigation strategies for combating the effects of global warming.

Studies on PET have a long history and have proposed several calculation methods, including the Penman–Monteith (Allen et al., 1998), Hargreaves (Hargreaves and Samani, 1985), and Priestly–Taylor methods (Priestley and Taylor, 1972), which can indirectly calculate PET using meteorological data (Aouissi et al., 2016). The Penman–Monteith method has been considered as a universal standard for estimating PET (Allen et al., 1998; Aouissi et al., 2016). However, this method requires five daily weather parameters that influence evaporation, namely, solar radiation, minimum and maximum air temperature, relative humidity, and wind speed. The other methods also provide acceptable results (Arnold et al., 1998). Considered the best method for estimating PET in the LP (Zhao et al., 2004), the Hargreaves method only depends on three monthly climate parameters, namely, mean, maximum, and minimum temperatures (Hargreaves and Samani, 1985).

General circulation models (GCMs) provide valuable information on long-term temperature projections at a global or sub-continental scale (IPCC, 2013). The Coupled Model Intercomparison Project Phase5 (CMIP5) of the World Climate Research Program provides the state-of-the-art multi-model dataset used by the Intergovernmental Panel on Climate Change for its fifth assessment report. Most of the extant GCMs have horizontal resolutions of a few hundred kilometers (Meehl et al., 2007), and several researchers have attempted to downscale CMIP5 model datasets to a 0.5° (approximately 55 km) (Brekke et al., 2013). However, spatial resolution limits the ability of GCM datasets to represent complex topography, land surface characteristics, and other processes in the climate system (Xu et al., 2016). Therefore, GCM datasets cannot draw realistic and reliable temperature change data at fine scales, which are required when developing suitable adaptation and mitigation strategies at the regional-to-local scale (Giorgi et al., 2009). Dynamic or statistical downscaling models for GCM data are necessary for downscaling a temperature dataset because these models add values to the data (Mosier et al., 2014; Xu et al., 2016). Dynamic downscaling requires numerous inputs and computational requirements (Brekke et al., 2013; Xu et al., 2016) and sometimes cannot represent reliable temperature change data at fine scales compared with statistical downscaling (Ahmed et al., 2013; Dosio et al., 2015; Xu et al., 2016). Therefore, statistical downscaling can generate a high spatial resolution temperature dataset for drawing PET information of the LP at a fine scale.

The statistical downscaling framework often involves regression and Delta downscaling methods. The former constructs multiple linear regression relationships between raw GCM data and station observations in the historical period, and then applies these relationships to future GCM grid outputs (Li et al., 2012b; Timm et al., 2015). This framework generates substantial climate element data at target stations in future periods, but cannot construct a high spatial resolution future climate dataset that prevents drawing detailed spatial variations at fine scales. The latter uses a low-resolution monthly time series and high-resolution reference climatology as inputs; the high-resolution climatology input must present a physically representative, fine-scale distribution of the meteorological variable over the landscape (Brekke et al., 2013; Mosier et al., 2014). Unlike the direct interpolation of low spatial resolution sources to a higher spatial resolution, the Delta downscaling process incorporates high-resolution orographic effects that are not represented in low-resolution input grids (Mosier et al., 2014).

Previous studies have assessed the future PET change and trend over the LP (Li et al., 2012a). However, these studies were conducted at the station scale, used the regression downscaling framework to obtain future climate data, and adopted a geo-statistical interpolation method to describe the spatial variations of PET. The limited amount of information on the detailed spatial variations of PET change and trend over the LP during future periods hinders the development of flexible adaptation and mitigation strategies to combat the effects of global warming in this region.

This study aims (1) to generate future monthly mean, maximum, and minimum temperature data with high spatial resolution using the Delta downscaling method and GCMs data, and (2) to calculate and assess future annual PET changes, trends, and their spatial variations based on the downscaled temperature data during 2011–2100.

## 2. Data and methods

### 2.1. Study area

The LP region is situated in North China (33.7°–41.3°N, 100.8°–114.6°E) and traversed by the upper–middle reaches of the Yellow River (Fig. 1). The region starts from the Taihang Mountains in the east, reaches the Riyue Mountains in the west, and borders on the Qinling and Yin Mountains in the south and north, respectively (Liu et al., 2016). The LP has a warm or temperate continental monsoon climate with extensive monsoonal influence. Approximately 60%–70% annual precipitation occurs in this region from June to September in the form of high-intensity storms (Wang et al., 2012). The annual mean temperature ranges from 3.6 °C in the northwest to 14.3 °C in the southeast. The region demonstrates a large diurnal temperature range throughout the year and faces dry and cold winters, hot and humid summers, rapid temperature reduction during autumn, and rapid temperature increase during spring. The annual potential evaporation in this area (865 mm–1274 mm) is estimated to exceed the precipitation level (Li et al., 2012a). The region spans arid, semiarid, and semi-humid zones and is considered as a semiarid-to-semihumid transitional zone that is sensitive to climate change (Liu and Sang, 2013).

### 2.2. Data collection

GCM monthly mean, maximum, and minimum temperature data were obtained from the downscaled CMIP5 dataset with a 0.5° resolution (http://gdo-dcp.ucllnl.org/downscaled_cmip_projections/). This dataset was processed from raw 28 GCM data using the bias-correction spatial disaggregation (BCSD) method described in Brekke et al. (2013). Table 1 lists the basic information of the 28 GCM models and the associated institutions. This dataset covers the period from January 1950 to December 2100; the data from 1950 to 2005 are historical data under the historical emissions scenario, while those from 2006 to 2100 are future data under future representative concentration pathway (RCP) scenarios (i.e., RCP2.6, RCP4.5, RCP6.0, and RCP8.5).

The high-resolution reference climatologies were presented as grid data with a 1 km (approximately 30″) resolution as suggested by the Chinese Ecosystem Research Network (CERN, www.cnern.org.cn). These climatologies were processed using spatial interpolation and geographic information systems that covered 740 national weather stations in China and a 1 km digital elevation model. These instruments covered each month from 1961 to 2000.

The surface observation data for the monthly mean, maximum, and minimum temperatures were obtained from 113 national weather stations in and around the LP (Fig. 1) (http://data.cma.cn/); these data were used to evaluate the downscaled monthly temperature grids from January 1991 to December 2005 (period of the available temperature data). The surface observation data for monthly pan evaporation were obtained from 26 evaporation pans belonging to the national weather stations in and around the LP (Fig. 1); these data were used to evaluate the calculated monthly

**Table 1**
Summary of 28 general circulation models from CMIP5.

| | Model acronym | Institution | References |
|---|---|---|---|
| 1 | ACCESS1.0 | Commonwealth Scientific and Industrial Research Organization and Bureau of Meteorology, Australia | Marsland et al. (2013) |
| 2 | BCC-CSM1.1 | Beijing Climate Center, China Meteorological Administration, China | Xin et al. (2013) |
| 3 | BCC-CSM1.1(m) | | Ren et al. (2016) |
| 4 | BNU-ESM | Beijing Normal University, China | Ji et al. (2014) |
| 5 | CanESM2 | Canadian Centre for Climate Modelling and Analysis, Canada | Chylek et al. (2011) |
| 6 | CESM1-BGC | NSF/DOE NCAR, USA | Long et al. (2013) |
| 7 | CESM1-CAM5 | | Neale et al. (2013) |
| 8 | CMCC-CM | Centro Euro-Mediterraneo per I Cambiamenti Climatici, Italy | Scoccimarro et al. (2011) |
| 9 | CNRM-CM5 | Centre National de Recherches Meteorologiques, Meteo-France, France | Voldoire et al. (2013) |
| 10 | CSIRO-MK-3.6.0 | Australian Commonwealth Scientific and Industrial Research Organization, Australia | Rotstayn et al. (2010) |
| 11 | EC-EARTH | EC-EARTH consortium, Europe | Hazeleger et al. (2012) |
| 12 | FGOALS-g2 | Institute of Atmospheric Physics, Chinese Academy of Sciences, China | Zhou et al. (2013) |
| 13 | FIO-ESM | The First Institution of Oceanography, SOA, China | Qiao et al. (2013) |
| 14 | GFDL-CM3 | NOAA Geophysical Fluid Dynamics Laboratory, USA | Donner et al. (2011) |
| 15 | GFDL-ESM2G | | Dunne et al. (2012) |
| 16 | GFDL-ESM2M | | Dunne et al. (2012) |
| 17 | GISS-E2-H-CC | NASA Goddard Institute for Space Studies, USA | Wang et al. (2015) |
| 18 | GISS-E2-R | | Schmidt et al. (2006) |
| 19 | GISS-E2-R-CC | | Wang et al. (2015) |
| 20 | HadCM3 | Met Office Hadley Centre, UK | Collins et al. (2001) |
| 21 | INMCM4.0 | Institute for Numerical Mathematics, Russia | Volodin et al. (2010) |
| 22 | IPSL-CM5A-LR | Institut Pierre-Simon Laplace, France | Dufresne et al. (2013) |
| 23 | MIROC4 h | Japan Agency for Marine-Earth Science and Technology, University of | Zhang et al. (2015) |
| 24 | MIROC5 | Tokyo, and National Institute for Environmental Studies (Japan) | Watanabe et al. (2010) |
| 25 | MIROC-ESM | | Watanabe et al. (2011) |
| 26 | MIROC-ESM-CHEM | | Watanabe et al. (2011) |
| 27 | MRI-CGCM3 | Meteorological Research Institute, Japan | Yukimoto et al. (2012) |
| 28 | NorESM1-M | Norwegian Climate Centre, Norway | Bentsen et al. (2013) |

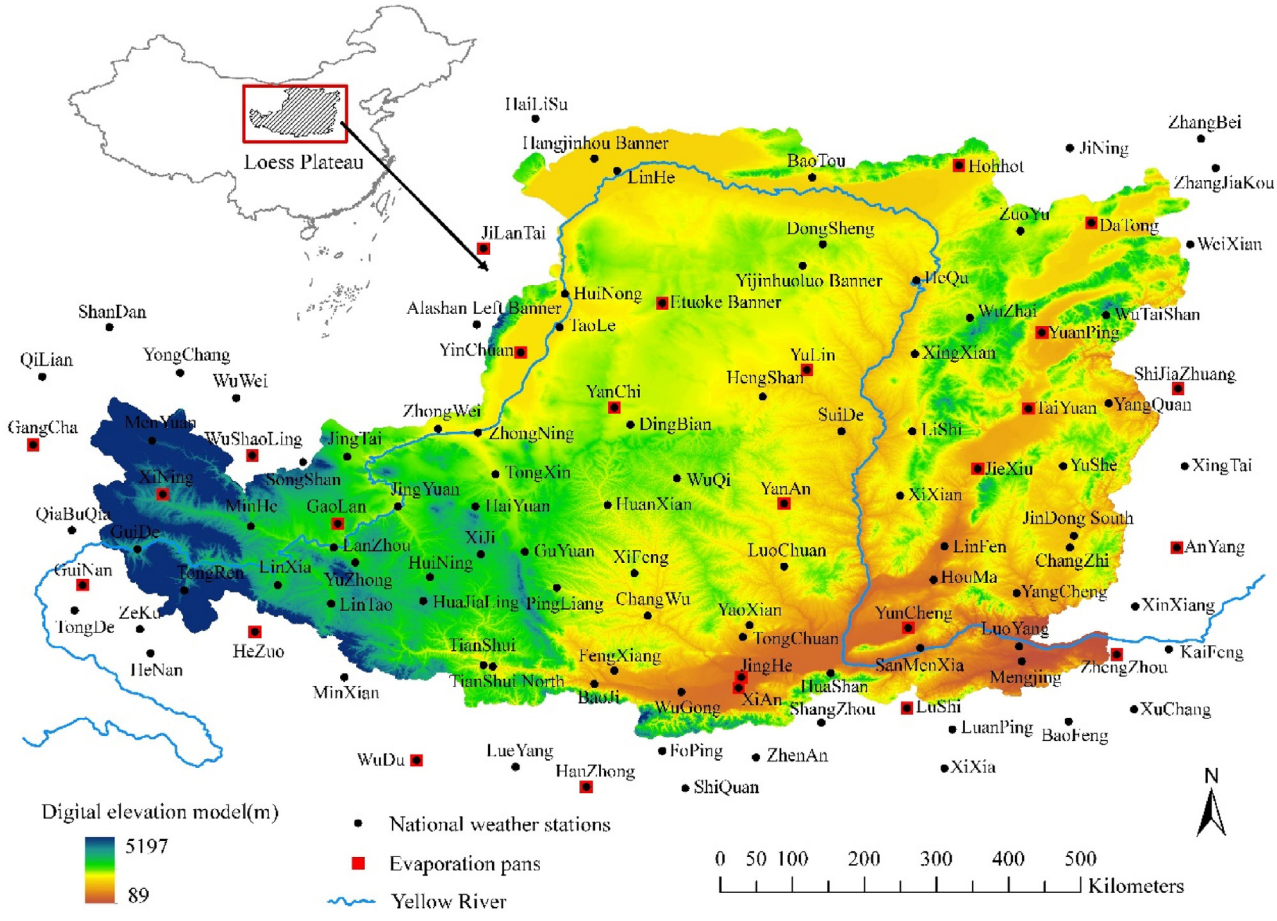


**Fig. 1.** Location and digital elevation model of Loess Plateau region in China, 131 national weather stations and 26 evaporation pans distributed in and around the region.

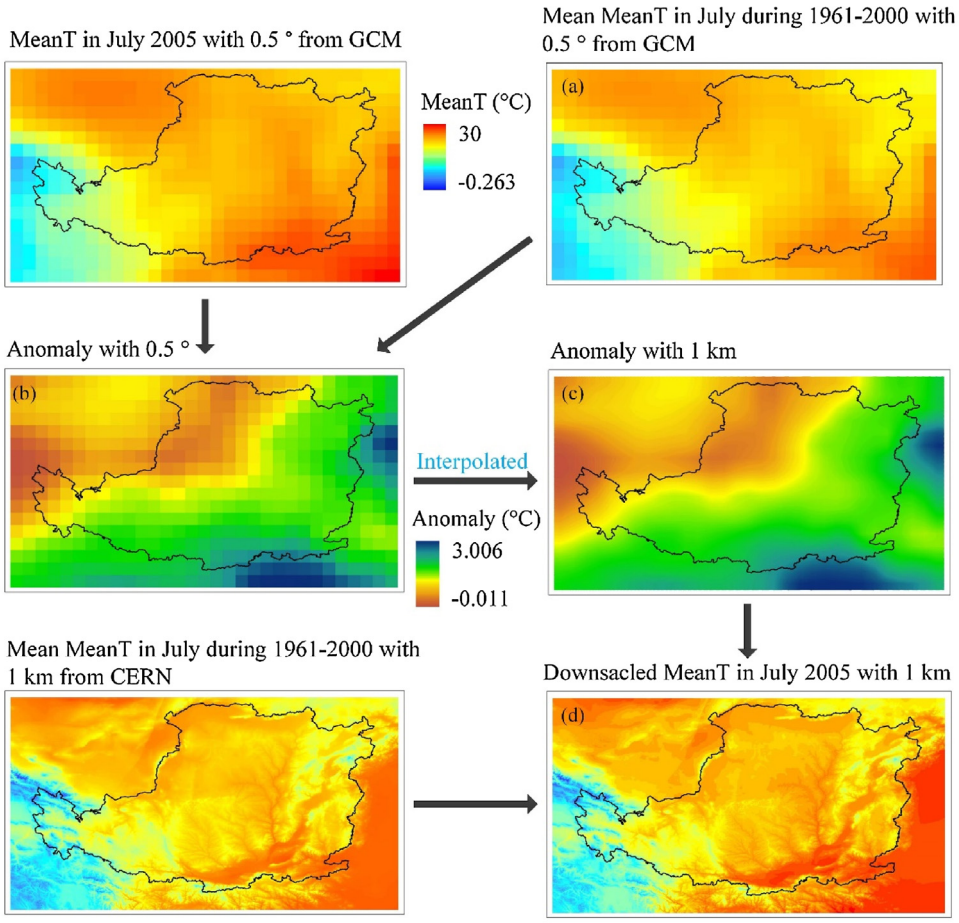


**Fig. 2.** Schematic illustration of spatial downscaling process. The downscaled mean temperature (MeanT) field is constructed from GCM data in July 2005.

PET grids from January 1985 to December 2005 (period of the available pan evaporation data).

### 2.3. Delta downscaling procedure

The Delta downscaling method was applied on the afore mentioned data to produce monthly mean, maximum, and minimum temperature grids with a 1 km resolution from January 1950 to December 2100. A part of the BCSD method, the Delta downscaling process has been described in many studies (Maurer et al., 2002; Ning et al., 2015; Wood et al., 2002). Fig. 2 shows a rectangular region (red zone in Fig. 1) that covers the LP region and illustrates the components and steps of the Delta downscaling process for determining mean temperature using the GCM 0.5° time series and CERN 30′′ climatology datasets. The first step (Fig. 2(a)) constructs a 0.5° climatology for each month from the 0.5° time-series dataset. The low-resolution climatology is produced using the 1961–2000 period, which is also used by CERN to construct its climatology data. A 0.5° anomaly (Fig. 2(b)) is then calculated. The anomaly for temperature is computed as the difference between the time series element and climatology. The anomaly is then interpolated to the 30′′ CERN grid using the spatial interpolation method (Fig. 2(c)). The final step (Fig. 2(d)) transforms the high-resolution anomaly back to an absolute surface by scaling this anomaly using the CERN climatology for the corresponding month. This transformation undoes the creation of the anomaly; therefore, addition is used for temperature.

The anomaly grid from the original to high-resolution coordinates, as illustrated in Fig. 2(c), can be interpolated using several interpolation methods, including nearest-neighbor, bilinear, cubic spline, and bicubic interpolations. The nearest-neighbor interpolation uses the values of nearby grids to estimate the value of the original grid. Bilinear interpolation fits a linear function over each interval on the original grid in one dimension and in another. Cubic spline interpolation fits a "natural" spline (i.e., without a tension parameter) to each interval. Bicubic interpolation is an extension of cubic interpolation that interpolates the value on a two-dimensional regular grid. The interpolated surface is smoother than the corresponding surfaces obtained via bilinear or nearest-neighbor interpolation. These four interpolation methods were conducted using the interp2 function of MATLAB.

### 2.4. Evaluation of the Delta downscaling method

The spatial downscaling process for temperature was conducted over the red zone in Fig. 1. Surface observation records from 113 national weather stations across the red zone were used to verify the accuracy of each downscaled grid. The observation records from January 1991 to December 2005 were used to verify the downscaled results.

The average model-performance error was quantified using mean absolute error (MAE), which is a more natural measure of average error compared with the root-mean-square error (Wang and Chen, 2014; Willmott and Matsuura, 2005). This accuracy estimator can be mathematically expressed as follows:

$$\mathrm{MAE} = \frac{1}{n} \times \sum_{i=1}^{n} \times |P_i - O_i|, \tag{1}$$

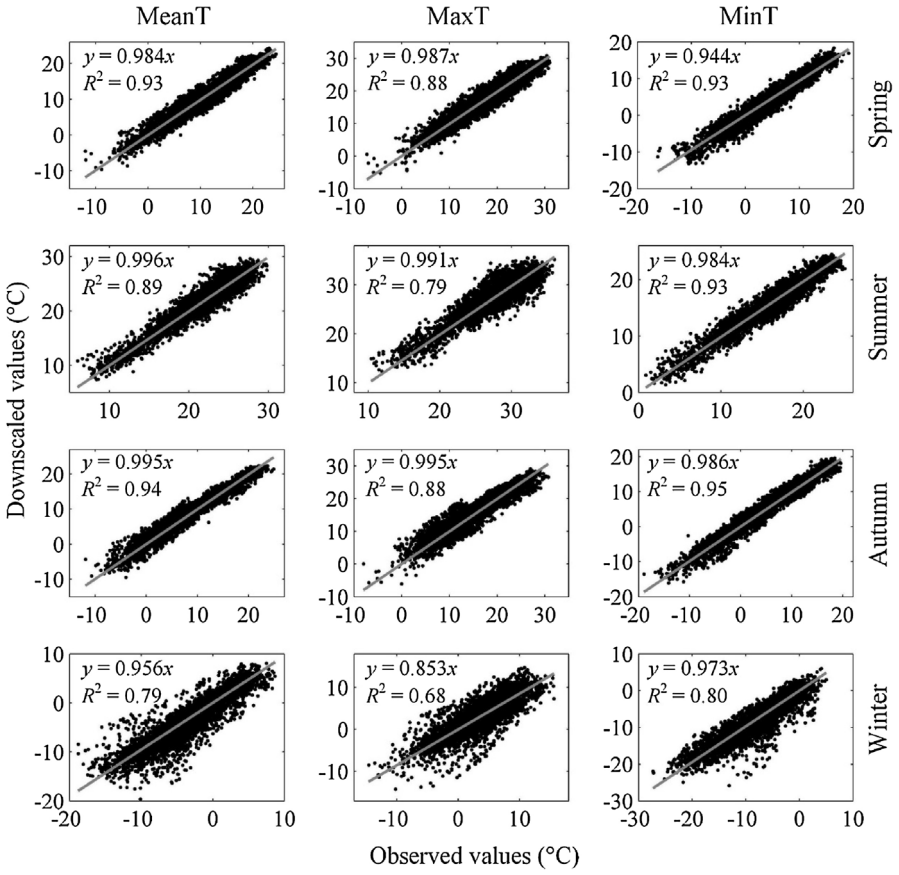


**Fig. 3.** Comparisons of the observed ($x$) and downscaled ($y$) values of monthly mean temperature (MeanT, °C), maximum temperature (MaxT, °C), and minimum temperature (MinT, °C) at the four seasons (spring: from March to May; summer: from June to August; autumn: from September to November; and winter: from December to February). The MeanT/MaxT and MinT values during 1/1991–12/2005 are downscaled from the NorESM1-M and GISS-E2-R models, respectively, using the bilinear interpolation method.

where $P_i$ and $O_i$ are the downscaled and observed values, respectively, and $n$ is the number of records of all validated stations.

### 2.5. Calculation of PET

Monthly PET (mm/month) is calculated via the Hargreaves method and by using monthly mean, maximum, and minimum temperatures. Several improvements were applied to the original equation (Hargreaves and Samani, 1982, 1985). The form used in this study was published in 1985 (Hargreaves and Samani, 1985) and expressed as follows:

$$\mathrm{PET} = 0.0023 \times \mathrm{S_0} \times (\mathrm{MaxT} - \mathrm{MinT})^{0.5} \times (\mathrm{MeanT} + 17.8), \quad (2)$$

where MaxT is the maximum air temperature for a specific month (°C), MinT is the minimum air temperature for a specific month (°C), MeanT is the mean air temperature for a specific month (°C), and $\mathrm{S_0}$ is the extra-terrestrial solar radiation (mm/month) at the top of the Earth's atmosphere on a horizontal surface (Allen et al., 1998). $\mathrm{S_0}$ can be calculated according to the solar constant, number of days in a year, latitude, and solar decimation. The detailed calculation procedure has been described in Allen et al. (1998) and Zhao et al. (2004).

### 2.6. Trend analysis methods

The significant trends in climatologic time series can be tested using parametric and non-parametric methods. Parametric trend tests require the data to be independent and normally distributed, while non-parametric trend tests only require independent data (Gocic and Trajkovic, 2013). Two non-parametric methods (Mann–Kendall and Sen's slope estimator tests) were used to detect the PET trends over the LP in each grid from 2011 to 2100. The Mann–Kendall test provides a measure ($Z_S$) that indicates whether the long-term change of a variable is significant or not (Atta-ur-Rahman and Dawood, 2016). A comparison analysis was conducted at the 95% confidence level. The time series trend was significant at the 95% confidence level when $|Z_S| > 1.96$. $Z_S > 1.96$ indicates a significant increase, while $Z_S < -1.96$ indicates a significant decrease. The magnitude of the PET trend was calculated via Sen's slope estimator test (Atta-ur-Rahman and Dawood, 2016).

## 3. Results

### 3.1. Evaluation of downscaled temperature and calculated PET

Table 2 shows the MAE between the downscaled and observed monthly MeanT, MaxT, and MinT under the four interpolation methods. The MAE under bilinear interpolation is the smallest for each GCM although such error slightly differs across the four interpolation methods. Similarly, the MAE under the bilinear interpolation ranges from 1.342 °C to 1.599 °C for monthly MeanT, from 1.715 °C to 1.978 °C for monthly MaxT, and from 1.336 °C to 5.527 °C for monthly MinT. The NorESM1-M model demonstrates the best performance in reproducing the monthly MeanT and MaxT over the LP, while the GISS-E2-R model demonstrates the best performance in reproducing the monthly MinT in the LP. The regression analysis reveals that the monthly temperature values downscaled by the most suitable GCMs data are close to the observed values at the four

**Table 2**
MAE between the observed and downscaled monthly MeanT, MaxT, and MinT from 113 national weather stations during 1/1991–12/2005.

| | Monthly MeanT (°C) | | | | Monthly MaxT (°C) | | | | Monthly MinT (°C) | | | |
|---|---|---|---|---|---|---|---|---|---|---|---|---|
| | Bicubic | Bilinear | Nearest | Spline | Bicubic | Bilinear | Nearest | Spline | Bicubic | Bilinear | Nearest | Spline |
| ACCESS1.0 | 1.460 | 1.458 | 1.462 | 1.460 | 1.824 | 1.822 | 1.824 | 1.824 | 1.442 | 1.439 | 1.444 | 1.442 |
| BCC-CSM1.1 | 1.419 | 1.418 | 1.419 | 1.419 | 1.780 | 1.779 | 1.781 | 1.780 | 1.415 | 1.414 | 1.416 | 1.415 |
| BCC-CSM1.1(m) | 1.449 | 1.447 | 1.450 | 1.449 | 1.819 | 1.818 | 1.820 | 1.819 | 1.458 | 1.457 | 1.460 | 1.458 |
| BNU-ESM | 1.429 | 1.429 | 1.430 | 1.429 | 1.822 | 1.821 | 1.822 | 1.822 | 1.392 | 1.391 | 1.394 | 1.392 |
| CanESM2 | 1.363 | 1.361 | 1.364 | 1.363 | 1.795 | 1.794 | 1.796 | 1.795 | 1.339 | 1.337 | 1.341 | 1.339 |
| CESM1-BGC | 1.434 | 1.432 | 1.435 | 1.434 | 1.753 | 1.751 | 1.754 | 1.753 | 1.482 | 1.480 | 1.483 | 1.482 |
| CESM1-CAM5 | 1.392 | 1.390 | 1.392 | 1.392 | 1.718 | 1.716 | 1.718 | 1.718 | 1.415 | 1.412 | 1.416 | 1.415 |
| CMCC-CM | 1.484 | 1.482 | 1.484 | 1.484 | 1.891 | 1.889 | 1.891 | 1.891 | 1.455 | 1.453 | 1.456 | 1.455 |
| CNRM-CM5 | 1.451 | 1.449 | 1.451 | 1.451 | 1.852 | 1.850 | 1.852 | 1.852 | 1.395 | 1.393 | 1.395 | 1.395 |
| CSIRO-MK-3.6.0 | 1.424 | 1.422 | 1.425 | 1.424 | 1.803 | 1.801 | 1.803 | 1.803 | 1.372 | 1.370 | 1.373 | 1.372 |
| EC-EARTH | 1.444 | 1.442 | 1.444 | 1.444 | 1.865 | 1.864 | 1.866 | 1.866 | 1.411 | 1.409 | 1.412 | 1.411 |
| FGOALS-g2 | 1.470 | 1.469 | 1.470 | 1.470 | 1.833 | 1.832 | 1.833 | 1.833 | 1.446 | 1.444 | 1.447 | 1.446 |
| FIO-ESM | 1.534 | 1.533 | 1.535 | 1.534 | 1.909 | 1.908 | 1.910 | 1.909 | 1.512 | 1.511 | 1.513 | 1.512 |
| GFDL-CM3 | 1.383 | 1.382 | 1.384 | 1.384 | 1.772 | 1.770 | 1.772 | 1.772 | 1.389 | 1.387 | 1.389 | 1.389 |
| GFDL-ESM2G | 1.415 | 1.413 | 1.416 | 1.415 | 1.727 | 1.725 | 1.729 | 1.728 | 1.476 | 1.474 | 1.478 | 1.476 |
| GFDL-ESM2M | 1.425 | 1.423 | 1.426 | 1.425 | 1.809 | 1.807 | 1.809 | 1.809 | 1.405 | 1.403 | 1.406 | 1.405 |
| GISS-E2-H-CC | 1.499 | 1.498 | 1.500 | 1.499 | 1.921 | 1.919 | 1.922 | 1.921 | 1.423 | 1.421 | 1.424 | 1.423 |
| GISS-E2-R | 1.347 | 1.346 | 1.347 | 1.347 | 1.729 | 1.727 | 1.730 | 1.729 | 1.338 | 1.336 | 1.338 | 1.338 |
| GISS-E2-R-CC | 1.407 | 1.406 | 1.407 | 1.407 | 1.802 | 1.800 | 1.802 | 1.802 | 1.409 | 1.407 | 1.410 | 1.409 |
| HadCM3 | 1.505 | 1.503 | 1.507 | 1.505 | 1.860 | 1.858 | 1.862 | 1.860 | 1.499 | 1.497 | 1.501 | 1.499 |
| INMCM4.0 | 1.564 | 1.562 | 1.565 | 1.564 | 1.940 | 1.939 | 1.942 | 1.941 | 1.536 | 1.532 | 1.538 | 1.536 |
| IPSL-CM5A-LR | 1.549 | 1.548 | 1.550 | 1.549 | 1.725 | 1.723 | 1.725 | 1.725 | 1.557 | 1.555 | 1.559 | 1.557 |
| MIROC4h | 1.471 | 1.469 | 1.472 | 1.471 | 1.828 | 1.825 | 1.830 | 1.828 | 1.461 | 1.459 | 1.462 | 1.461 |
| MIROC5 | 1.446 | 1.445 | 1.447 | 1.446 | 1.847 | 1.845 | 1.848 | 1.847 | 5.528 | 5.527 | 5.527 | 5.528 |
| MIROC-ESM | 1.379 | 1.377 | 1.380 | 1.379 | 1.788 | 1.786 | 1.788 | 1.788 | 1.388 | 1.386 | 1.391 | 1.388 |
| MIROC-ESM-CHEM | 1.600 | 1.599 | 1.600 | 1.600 | 1.980 | 1.978 | 1.980 | 1.980 | 1.598 | 1.597 | 1.599 | 1.598 |
| MRI-CGCM3 | 1.571 | 1.570 | 1.571 | 1.571 | 1.949 | 1.947 | 1.950 | 1.949 | 1.553 | 1.551 | 1.553 | 1.553 |
| NorESM1-M | 1.343 | 1.342 | 1.344 | 1.343 | 1.717 | 1.715 | 1.718 | 1.717 | 1.341 | 1.339 | 1.341 | 1.341 |

Bicubic, Bilinear, Nearest, and Spline represent the bicubic, bilinear, nearest-neighbor, and cubic spline interpolations, respectively.

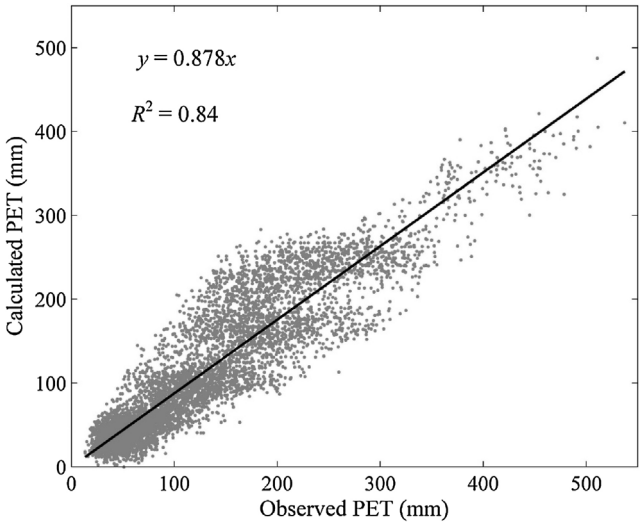


**Fig. 4.** Comparisons of the observed ($x$) and calculated ($y$) values of potential evapotranspiration (PET, mm) during 1/1985–12/2005.

seasons (Fig. 3). Although the monthly PET values calculated by the most accurate MeanT, MaxT, and MinT values are slightly smaller than the observed values, the statistical indicators between these values present a high evaluation for calculating the monthly PET (Fig. 4).

### 3.2. Spatiotemporal changes in PET

As mentioned in Section 3.1, the monthly PET during the 1950–2100 period was calculated by the MeanT, MaxT, and MinT, and the temperature values were downscaled by the most suitable GCM data using the bilinear interpolation method. A reference period (1961–1990) was set, and the future period (2011–2100) was divided into three periods (2011–2040, 2041–2070, and 2071–2100) to assess the spatiotemporal change and trend of annual PET in the future period.

Fig. 5 shows the spatial patterns of mean annual PET changes in the future period (2011–2100) under the four RCP scenarios relative to the reference period (1961–1990). Under each RCP, the zones that showed the largest changes were located in high-elevation regions, such as Wutai Mountain in the northeast, Hua Mountain in the south, and Qilian Mountains in the west. Table 3 shows the corresponding Min, Max, Mean, and coefficient of variation (CV) for each spatial distribution in Fig. 5. The CV indicates that RCP8.5 shows the largest spatial variation (10.9%), while RCP2.6 shows the smallest spatial variation (9.2%). The difference between Max and Min indicates that RCP8.5 shows the most extreme spatial variation (20.6%; ranging from 11.9% to 32.6%), while RCP2.6 shows the most moderate spatial variation (10.9%; ranging from 7.6% to 18.5%). The Mean indicates that the PET over the LP changes by 9.5% for RCP2.6, 10.8% for RCP4.5, 10.1% for RCP6.0, and 14.1% for RCP8.5.

Fig. 6 shows the spatial patterns of the mean annual PET changes in 2011–2040, 2041–2070, and 2071–2100 under the four RCP scenarios relative to the reference period (1961–1990). During each period, the zones with the largest PET change were located in some high-elevation regions under all RCP scenarios as shown in the 2011–2100 period. Table 3 shows the corresponding Min, Max, Mean, and CV for each spatial distribution in Fig. 6. The CV indicates that RCP4.5 shows the largest spatial variation in 2011–2040 (21.8%), while RCP6.0 shows the smallest spatial variation in 2071–2100 (8.3%). The difference between Max and Min indicates that RCP8.5 shows the most extreme spatial variation in 2071–2100 (31.9%; ranging from 20.6% to 52.5%), while RCP6.0 shows the most moderate spatial variation in 2011–2040 (9.7%; ranging from 1.8% to 11.5%). The Mean indicates that the averaged PET change over the LP increases with time under each RCP scenario in the future periods.

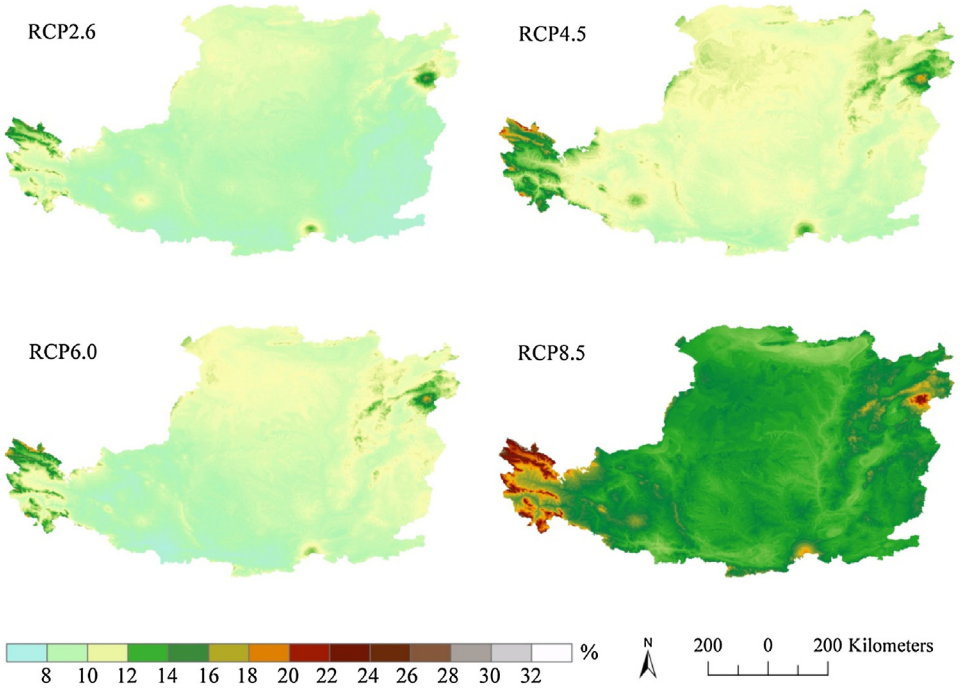


**Fig. 5.** Geographic distributions of the changes in the mean annual PET (%) from the reference period (1961–1990) to the future period (2011–2100) under four emission scenarios.

**Table 3**
Spatial distribution characteristics of mean annual PET change (%) in the future periods relative to the reference period (1961–1990).

| | 2011–2040 | | | | 2041–2070 | | | | 2071–2100 | | | | 2011–2100 | | | |
|---|---|---|---|---|---|---|---|---|---|---|---|---|---|---|---|---|
| | RCP2.6 | RCP4.5 | RCP6.0 | RCP8.5 | RCP2.6 | RCP4.5 | RCP6.0 | RCP8.5 | RCP2.6 | RCP4.5 | RCP6.0 | RCP8.5 | RCP2.6 | RCP4.5 | RCP6.0 | RCP8.5 |
| Min | 3.9 | 2.3 | 1.8 | 3.5 | 7.8 | 9.3 | 5.7 | 10.3 | 9.8 | 12.7 | 13.3 | 20.6 | 7.6 | 8.7 | 7.3 | 11.9 |
| Max | 14.8 | 14.1 | 11.5 | 14.2 | 19.2 | 25.3 | 19.5 | 31.2 | 23.2 | 32.6 | 33.2 | 52.5 | 18.5 | 24.0 | 21.4 | 32.6 |
| Mean | 6.2 | 5.0 | 4.3 | 5.4 | 9.7 | 11.7 | 9.0 | 12.9 | 12.7 | 15.8 | 17.0 | 23.9 | 9.5 | 10.8 | 10.1 | 14.1 |
| CV | 15.3% | 21.8% | 19.7% | 17.5% | 9.1% | 9.9% | 12.7% | 12.9% | 9.5% | 9.2% | 8.3% | 9.2% | 9.2% | 10.5% | 10.4% | 10.9% |

Min, Max, Mean, and CV are the minimum, maximum, mean, and coefficient of variation, respectively.

### 3.3. Trend analysis in PET

Mann–Kendall and Sen's slope estimator tests were conducted at each grid over the LP. Fig. 7 maps the spatial patterns of annual PET trend during 2011–2100 (i.e., 90-year span) under the four RCP scenarios, while Table 4 lists the corresponding statistical indexes (Min, Max, Mean, and CV) and area ratios (AR) of the significant trend zones over the entire LP region. The Mann–Kendall test reveals that the annual PET during 2011–2100 at each grid over the LP demonstrates a significantly increasing trend under each RCP scenario, that is, the AR under each RCP scenario is equal to 100% at the 95% confidence level. The CV indicates that RCP2.6 shows the largest spatial variation (17.6%), while RCP8.5 shows the smallest spatial variation (7.1%). The difference between Max and Min indicates that RCP8.5 shows the most extreme spatial variation (14.2 mm/10yr; ranging from 22.9 mm/10yr to 37.1 mm/10yr), while RCP2.6 shows the most moderate spatial variation (12.9 mm/10yr; ranging from 3.1 mm/10yr to 16 mm/10yr). The Mean indicates that the averaged magnitude of PET trend over the LP increases along with emission intensity; the averaged magnitude is equal to 10.4 mm/10yr for RCP2.6, 17.7 mm/10yr for RCP4.5, 21.0 mm/10yr for RCP6.0, and 29.7 mm/10yr for RCP8.5.

Fig. 8 maps the spatial patterns of annual PET trends in the three future periods (i.e., 30-year span) under the four RCP scenarios, while Table 4 lists the corresponding indexes (Min, Max, Mean, CV, and AR). The trend significantly increases under each scenario during 2011–2040. Specifically, the significantly increasing trend ranges from 10.9 mm/10yr to 41.9 mm/10yr with a mean of 26.5 mm/10yr for RCP2.6, from 9.8 mm/10yr to 48.7 mm/10yr with a mean of 29.1 mm/10yr for RCP4.5, from 7.7 mm/10yr to 29.3 mm/10yr with a mean of 18.5 mm/10yr for RCP6.0, and from 7.4 mm/10yr to 30.9 mm/10yr with a mean of 20.2 mm/10yr for RCP8.5. This trend is observed in most of the LP region with 97.7% and 97.4% ARs under RCP2.6 and RCP4.5, respectively, in the west and north of the LP region with 36.3% AR under RCP6.0, and in the west and east of the LP region with 30% AR under RCP8.5. The trend also increases significantly under the three scenarios during 2041–2070. Specifically, the significantly increasing trend ranges from 12.7 mm/10yr to 49.3 mm/10yr with a mean of 29.9 mm/10yr for RCP4.5, from 10 mm/10yr to 42.5 mm/10yr with a mean of 27.1 mm/10yr for RCP6.0, and from 12.9 mm/10yr to 46.2 mm/10yr with a mean of 28.5 mm/10yr for RCP8.5. This trend is observed in most of the LP region with 99.9%, 76.9%, and 95.7% ARs under RCP4.5, RCP6.0, and RCP8.5, respectively. During this same period, the trend significantly decreases under the RCP2.6 scenario and it ranges from 8.6 mm/10yr to 19.8 mm/10yr with a mean of 14.8 mm/10yr. This trend is observed in north of the LP with a 0.3% AR. The trend significantly increases under the three scenarios during 2071–2100; Specifically, the significantly increasing trend ranges from 7.5 mm/10yr to 33 mm/10yr with a mean of 18.7 mm/10yr for RCP4.5, from 12.8 mm/10yr to 50.5 mm/10yr with a mean of 26.7 mm/10yr for RCP6.0, and from 20.5 mm/10yr to 55.8 mm/10yr with a mean of 37.2 mm/10yr for RCP8.5. This trend

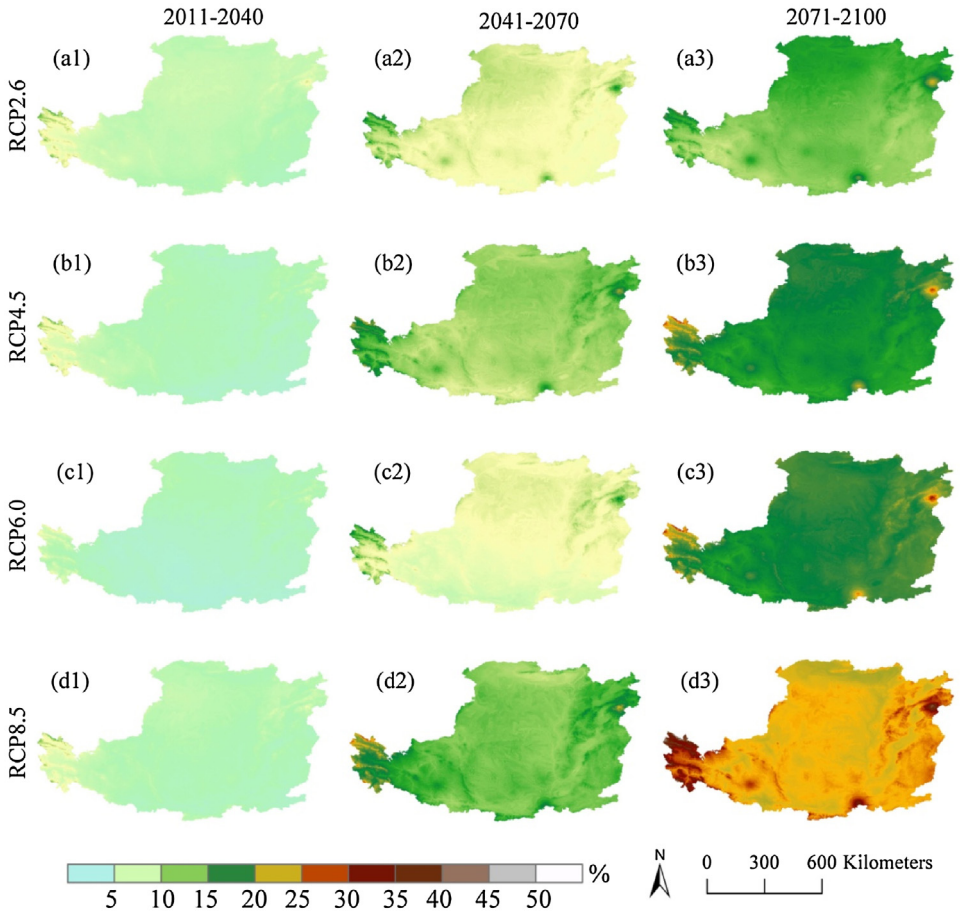


**Fig. 6.** Geographic distributions of the changes in the mean annual PET (%) from the reference period (1961–1990) to beginning-of-century (a1, b1, c1, and d1: 2011–2040), mid-century (a2, b2, c2, and d2: 2041–2070), and end-of-century (a3, b3, c3, and d3: 2071–2100) under four emission scenarios (rows).

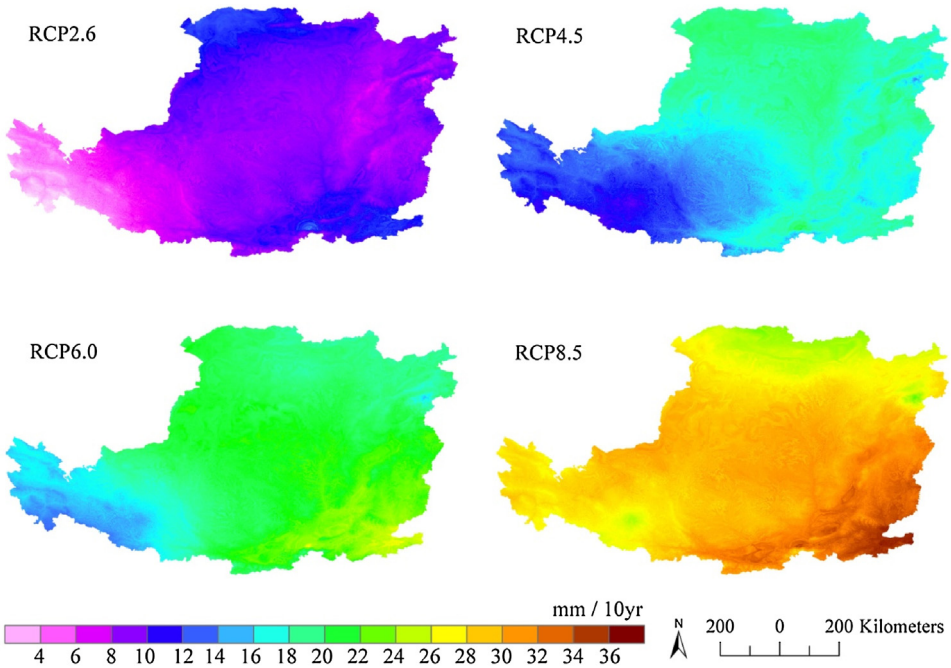


**Fig. 7.** Geographic distributions of the trend for the annual PET (mm/10yr) during 2011–2100 under four emission scenarios.

**Table 4**
Spatial distribution characteristics of significant trend (mm/10yr) in annual PET in the future periods.

| | 2011–2040 | | | | 2041–2070 | | | | 2071–2100 | | | | 2011–2100 | | | |
|---|---|---|---|---|---|---|---|---|---|---|---|---|---|---|---|---|
| | RCP2.6 | RCP4.5 | RCP6.0 | RCP8.5 | RCP2.6 | RCP4.5 | RCP6.0 | RCP8.5 | RCP2.6 | RCP4.5 | RCP6.0 | RCP8.5 | RCP2.6 | RCP4.5 | RCP6.0 | RCP8.5 |
| Min | 10.9 | 9.8 | 7.7 | 7.4 | **8.6** | 12.7 | 10.0 | 12.9 | **10.2** | 7.5 | 12.8 | 20.5 | 3.1 | 10.9 | 14.0 | 22.9 |
| Max | 41.9 | 48.7 | 29.3 | 30.9 | **19.8** | 49.3 | 42.5 | 46.2 | **29.4** | 33.0 | 50.5 | 55.8 | 16.0 | 23.1 | 27.8 | 37.1 |
| Mean | 26.5 | 29.1 | 18.5 | 20.2 | **14.8** | 29.9 | 27.1 | 28.5 | **18.7** | 18.7 | 26.7 | 37.2 | 10.4 | 17.7 | 21.0 | 29.7 |
| CV | 18.2% | 23.2% | 15.8% | 16.7% | 10.4% | 20.9% | 14.9% | 17.5% | 11.6% | 14% | 16.2% | 14.1% | 17.6% | 13.0% | 10.3% | 7.1% |
| AR | 97.7% | 97.4% | 36.3% | 30.0% | 0.3% | 99.9% | 76.9% | 95.7% | 1.2% | 10.3% | 97.5% | 100% | 100% | 100% | 100% | 100% |

AR is the area ratio of the significant trend zones to the entire LP region. The boldface numbers indicate significant decreases at the 95% confidence level.

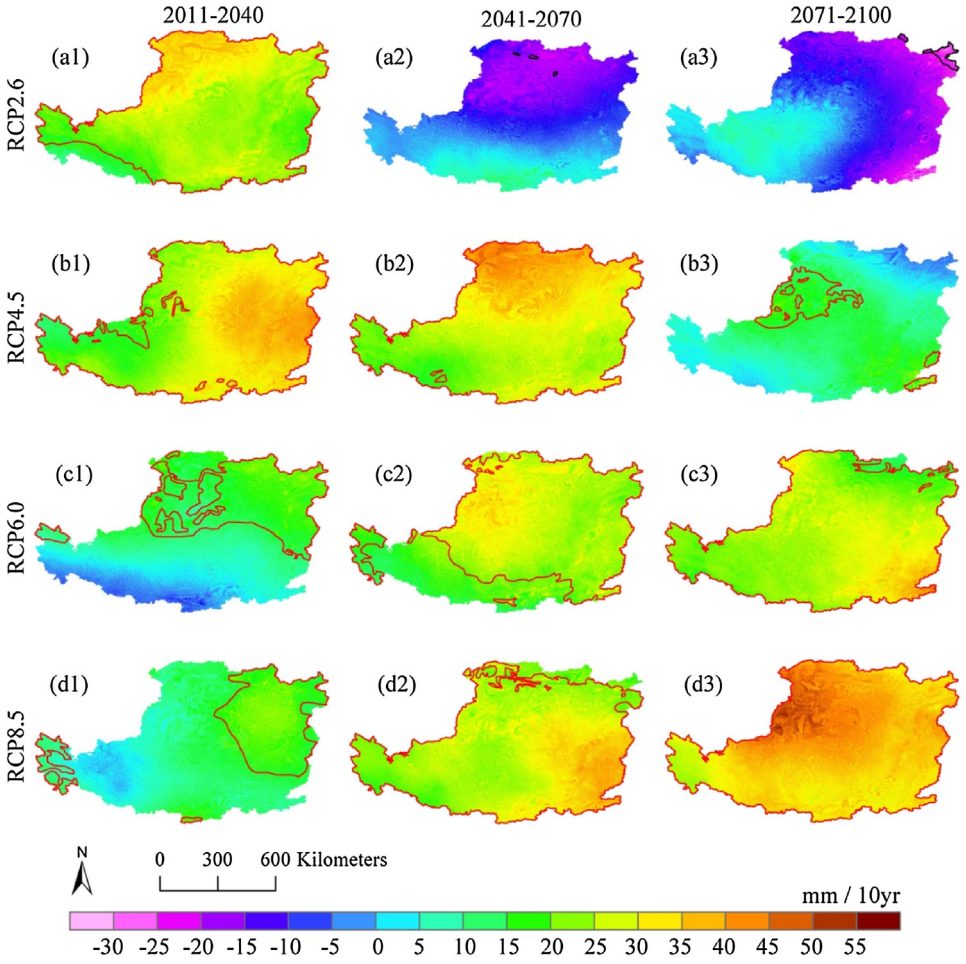


**Fig. 8.** Geographic distributions of the trend for the annual PET (mm/10yr) during the future periods (columns) under four emission scenarios (rows). The red zone indicates where the trend significantly increases at the 95% confidence level, and the black zone indicates where the trend significantly decreases at the 95% confidence level. (For interpretation of the references to colour in this figure legend, the reader is referred to the web version of this article.)

is observed in the southeast and northwest of the LP with 10.3% and 97.5% ARs for RCP4.5 and RCP6.0, respectively. This trend is observed across the entire LP region under the RCP8.5 scenario. During this same period, the trend significantly decreases under the RCP2.6 scenario; it ranges from 10.2 mm/10yr to 29.4 mm/10yr with a mean of 18.7 mm/10yr and is located in northeast of the LP region with 1.2% AR. According to the CV analysis, RCP4.5 shows the largest spatial variation in 2011–2040 (23.2%), while RCP2.6 shows the smallest spatial variation in 2041–2070 (10.4%).

## 4. Summary and discussion

Although the significant changes in the PET trend over the LP have been studied in the literature (Li et al., 2012a), previous studies were performed at the station scale and did not provide the magnitude of PET trend. This study assesses the PET changes and trends over the LP in future periods (i.e., 2011–2040, 2041–2070, 2071–2100, and 2011–2100) based on the high spatiotemporal resolution future temperature data generated through the Delta downscaling method and GCMs data of CMIP5. These spatiotemporal results represent the PET changes and trends over the LP in detail and provide insights for developing flexible adaptation and mitigation strategies to combat the effects of global warming in this region.

The PET changes in each future period demonstrate a very strong spatial variability (Figs. 5 and 6, Table 3). Therefore, high spatial resolution temperature data are crucial in capturing PET variation at the fine scale. Large PET changes are also observed in some high-elevation regions (Figs. 5 and 6). Based on the PET equation (i.e., Eq. (2)), these changes can be attributed to the fact that the

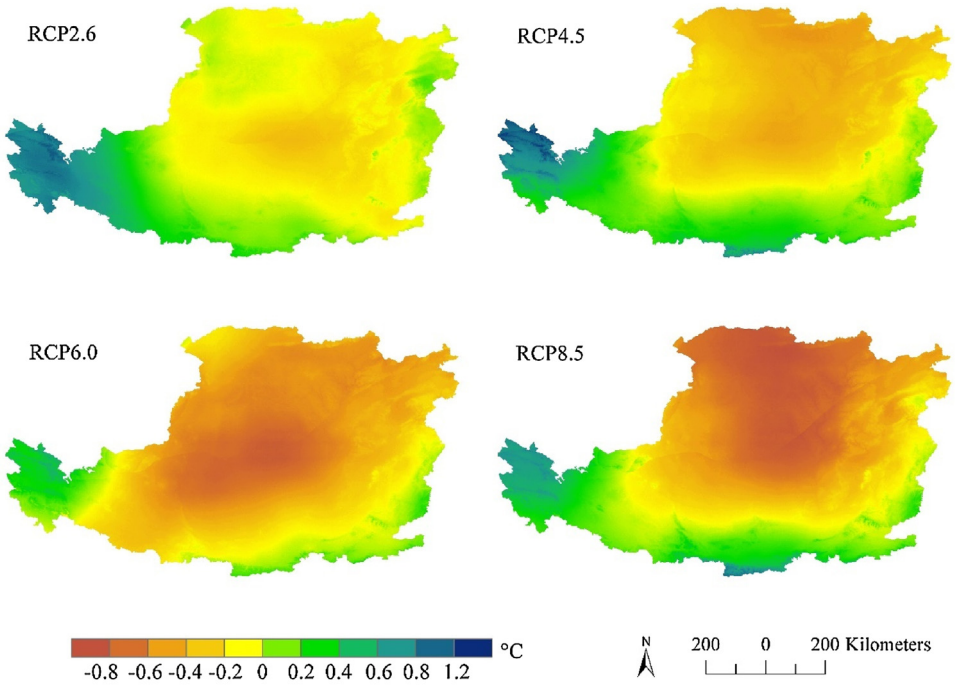


**Fig. 9.** Geographic distributions of the changes in the differences between MaxT and MinT (°C) from the reference period (1961–1990) to the future period (2011–2100) under four emission scenarios.

high-elevation regions show a higher increment in the difference between MaxT and MinT than the low-elevation regions, especially for the Qilian Mountains located west of the LP region (Fig. 9). Moreover, the average annual PET over the LP region will increase by 12.7%–23.9% from 1961 to 1990 to the end of this century (2071–2100) (Table 3), while Wang and Chen (2014) predicted that the average annual precipitation over the LP region would increase by 10% in the same period. These results imply an increasing trend of water shortage over the LP region at the end of the century. Such accelerating water shortage may further decrease the crop yields and threaten the functioning of the native vegetation ecosystem. Therefore, the necessary adaptation and mitigation strategies must be adopted in the future to address these issues.

The magnitude of PET trend in each future period also demonstrates a very strong spatial variability (Figs. 7 and 8, Table 4). The significant trends in PET are mapped over the LP, and their distributions present diverse characteristics, especially in terms of location and AR (Figs. 7 and 8). The Delta downscaling method reveals that the above detailed spatial results differ from those presented in other climate change studies, which have mapped the climate variables (e.g., temperature, precipitation, and PET) based on multiple weather stations data and by using geo-statistical interpolation methods, such as inverse distance weighted interpolation (Li et al., 2012a) and ordinary kriging interpolation (Atta-ur-Rahman and Dawood, 2016). Overall, unlike those from other studies, the spatial results in this study can draw the detailed orographic effects on MeanT, MaxT, MinT, and PET, as well as provide highly accurate information, such as location, AR, and other statistical indexes. These differences can be attributed to two reasons. First, other studies directly interpolated their station data to reveal the spatial patterns of climate variables, while this study employed the Delta downscaling framework to detect such patterns. Second, this study adopted a high-resolution climatology that represented an orographic effect with a 1 km spatial resolution in the Delta downscaling framework.

The significant PET trends in each future period (2011–2040, 2041–2070, and 2071–2100) under the four RCP scenarios show diverse spatial patterns and statistical results (Fig. 8 and Table 4). By comparing the three major uncertainties in climate predictions that result from future natural fluctuations, model responses, and emission scenarios (Hawkins and Sutton, 2009, 2011), the above diverseness can be attributed to inter-GCM (i.e., the spread of changes among GCMs under the same RCP scenario) and scenarios uncertainties (Ning and Bradley, 2015, 2016). Given that this study adopted the data from two GCMs (i.e., NorESM1-M and GISS-E2-R models) to calculate the high-resolution future PET under the four RCP scenarios, the inter-GCM and scenarios uncertainties have a conjunction effect on the PET trends. Moreover, the PET trends under the RCP2.6 and RCP4.5 scenarios in 2011–2040 are larger than those under the RCP6.0 and RCP8.5 scenarios (Table 4), which implies that the uncertainties resulting from the NorESM1-M and GISS-E2-R models are greater than those resulting from the different scenarios in this period. By contrast, in 2071–2100, the total uncertainties increase along with the emission scenarios, and the largest trend is observed under the RCP8.5 scenario.

This study employed the Delta downscaling framework to generate the monthly mean, maximum, and minimum temperatures with a 1 km spatial resolution from January 1950 to December 2100 based on the GCM dataset with a 0.5° spatial resolution and high-resolution climatology representing an orographic effect. The MAE and regression analysis between the downscaled data and the independent surface station observations reflected the excellent performance of the Delta downscaling method (Table 2 and Fig. 3). Wang and Chen (2014) used the Delta method to downscale raw 35 GCM data to a 0.5° spatial resolution; the MAE of monthly mean temperature ranged from 1.6 °C to 5.7 °C with a mean of 3.2 °C. Compared with those in Wang and Chen (2014), the MAE of monthly mean temperature in this study was smaller and ranged from 1.34 °C to 1.6 °C with a mean of 1.45 °C (Table 2). Wang and Chen (2014) also identified EC-EARTH as the model with the smallest MAE; this model generated a 0.5° spatial resolution temperature in China. By contrast, this study identifies the NorESM1-M and GISS-E2-R models as the best models for reproducing the monthly mean/maximum and minimum temperatures over the LP, respec-

tively. These differences may be attributed to the fact that this study adopted high-resolution climatology with a 1 km spatial resolution for downscaling and used surface station observations to evaluate the downscaled results. These differences emphasized the importance of high-resolution climatology and evaluation data in using the Delta downscaling framework. Until now, WorldClim (Mosier et al., 2014) and the employed climatology in this study are the best available high-resolution climatologies in the world and in China, respectively. Both climatologies have a 1 km spatial resolution in the Delta downscaling framework.

## Acknowledgements

This work was supported by National Natural Science Foundation of China (41601058), CAS "Light of West China" Program (XAB2015B07), China Special Fund for Meteorological Research in the Public Interest (Major projects) (GYHY201506001-3), and Key cultivation project of Chinese Academy of Sciences "The promotion and management of ecosystem functions of restored vegetation in Loess Plateau, China". The authors are grateful to the World Climate Research Programme's Working Group on Coupled Modelling, which is responsible for CMIP, and the authors thank the climate modeling groups (listed in Table 1 of this paper) for producing and making available their model output. For CMIP the U.S. Department of Energy's Program for Climate Model Diagnosis and Intercomparison provides coordinating support and led development of software infrastructure in partnership with the Global Organization for Earth System Science Portals. In addition, the authors wish to thank two anonymous reviewers for their constructive suggestions to improve the quality of this article.

## References

Ahmed, K.F., Wang, G., Silander, J., Wilson, A.M., Allen, J.M., Horton, R., Anyah, R., 2013. Statistical downscaling and bias correction of climate model outputs for climate change impact assessment in the U.S. northeast. Glob. Planet Change 100, 320–332.

Allen, R.G., Pereira, L.S., Raes, D., Smith, M., 1998. Crop Evapotranspiration-Guidelines for Computing Crop Water Requirements-FAO Irrigation and Drainage Paper 56, vol. 300. FAO, Rome, pp. D05109.

Aouissi, J., Benabdallah, S., Chabaâne, Z.L., Cudennec, C., 2016. Evaluation of potential evapotranspiration assessment methods for hydrological modelling with SWAT–Application in data-scarce rural Tunisia. Agric. Water Manage. 174, 39–51.

Arnold, J.G., Srinivasan, R., Muttiah, R.S., Williams, J.R., 1998. Large area hydrologic modeling and assessment part I: model development1. J. Am. Water Resour. Assoc. 34, 73–89.

Atta-ur-Rahman, Dawood, M., 2016. Spatio-statistical analysis of temperature fluctuation using Mann–Kendall and Sen's slope approach. Clim. Dyn., http://dx.doi.org/10.1007/s00382-016-3110-y.

Bentsen, M., Bethke, I., Debernard, J.B., Iversen, T., Kirkevåg, A., Seland, Ø., Drange, H., Roelandt, C., Seierstad, I.A., Hoose, C., Kristjánsson, J.E., 2013. The norwegian earth system model, norESM1-M – part 1: description and basic evaluation of the physical climate. Geosci. Model Dev. 6, 687–720.

Bi, H., Liu, B., Jie, W., Yun, L., Chen, Z., Cui, Z., 2009. Effects of precipitation and landuse on runoff during the past 50 years in a typical watershed in Loess Plateau, China. Int. J. Sediment Res. 24, 352–364.

Brekke, L., Thrasher, B., Maurer, E., Pruitt, T., 2013. Downscaled CMIP3 and CMIP5 Climate and Hydrology Projections: Release of Downscaled CMIP5 Climate Projections, Comparison with Preceding Information, and Summary of User Needs. US Dept. of the Interior, Bureau of Reclamation, Technical Services Center, Denver, Colorado.

Chylek, P., Li, J., Dubey, M.K., Wang, M., Lesins, G., 2011. Observed and model simulated 20th century arctic temperature variability: canadian earth system model CanESM2. Atmos. Chem. Phys. Discuss. 2011, 22893–22907.

Collins, M., Tett, S.F.B., Cooper, C., 2001. The internal climate variability of HadCM3, a version of the Hadley Centre coupled model without flux adjustments. Clim. Dyn. 17, 61–81.

Donner, L.J., Wyman, B.L., Hemler, R.S., Horowitz, L.W., Ming, Y., Zhao, M., Golaz, J.-C., Ginoux, P., Lin, S.-J., Schwarzkopf, M.D., Austin, J., Alaka, G., Cooke, W.F., Delworth, T.L., Freidenreich, S.M., Gordon, C.T., Griffies, S.M., Held, I.M., Hurlin, W.J., Klein, S.A., Knutson, T.R., Langenhorst, A.R., Lee, H.-C., Lin, Y., Magi, B.I., Malyshev, S.L., Milly, P.C.D., Naik, V., Nath, M.J., Pincus, R., Ploshay, J.J., Ramaswamy, V., Seman, C.J., Shevliakova, E., Sirutis, J.J., Stern, W.F., Stouffer, R.J., Wilson, R.J., Winton, M., Wittenberg, A.T., Zeng, F., 2011. The dynamical core, physical parameterizations, and basic simulation characteristics of the atmospheric component AM3 of the GFDL global coupled model CM3. J. Clim. 24, 3484–3519.

Dosio, A., Panitz, H.-J., Schubert-Frisius, M., Lüthi, D., 2015. Dynamical downscaling of CMIP5 global circulation models over CORDEX-Africa with COSMO-CLM: evaluation over the present climate and analysis of the added value. Clim. Dyn. 44, 2637–2661.

Dufresne, J.-L., Foujols, M.-A., Denvil, S., Caubel, A., Marti, O., Aumont, O., Balkanski, Y., Bekki, S., Bellenger, H., Benshila, R., Bony, S., Bopp, L., Braconnot, P., Brockmann, P., Cadule, P., Cheruy, F., Codron, F., Cozic, A., Cugnet, D., de Noblet, N., Duvel, J.-P., Ethé, C., Fairhead, L., Fichefet, T., Flavoni, S., Friedlingstein, P., Grandpeix, J.-Y., Guez, L., Guilyardi, E., Hauglustaine, D., Hourdin, F., Idelkadi, A., Ghattas, J., Joussaume, S., Kageyama, M., Krinner, G., Labetoulle, S., Lahellec, A., Lefebvre, M.-P., Lefevre, F., Levy, C., Li, Z.X., Lloyd, J., Lott, F., Madec, G., Mancip, M., Marchand, M., Masson, S., Meurdesoif, Y., Mignot, J., Musat, I., Parouty, S., Polcher, J., Rio, C., Schulz, M., Swingedouw, D., Szopa, S., Talandier, C., Terray, P., Viovy, N., Vuichard, N., 2013. Climate change projections using the IPSL-CM5 earth system model: from CMIP3 to CMIP5. Clim. Dyn. 40, 2123–2165.

Dunne, J.P., John, J.G., Adcroft, A.J., Griffies, S.M., Hallberg, R.W., Shevliakova, E., Stouffer, R.J., Cooke, W., Dunne, K.A., Harrison, M.J., Krasting, J.P., Malyshev, S.L., Milly, P.C.D., Phillipps, P.J., Sentman, L.T., Samuels, B.L., Spelman, M.J., Winton, M., Wittenberg, A.T., Zadeh, N., 2012. GFDL's ESM2 global coupled Climate–Carbon earth system models. part I: physical formulation and baseline simulation characteristics. J. Clim. 25, 6646–6665.

Giorgi, F., Jones, C., Asrar, G.R., 2009. Addressing climate information needs at the regional level: the CORDEX framework. World Meteorol. Org. Bull. 58, 175–183.

Gocic, M., Trajkovic, S., 2013. Analysis of changes in meteorological variables using Mann-Kendall and Sen's slope estimator statistical tests in Serbia. Glob. Planet Change 100, 172–182.

Hargreaves, G.H., Samani, Z.A., 1982. Estimating potential evapotranspiration. J. Irrig. Drain. Div. 108, 225–230.

Hargreaves, G.H., Samani, Z.A., 1985. Reference crop evapotranspiration from temperature. Appl. Eng. Agric. 1, 96–99.

Hawkins, E., Sutton, R., 2009. The potential to narrow uncertainty in regional climate predictions. Bull. Am. Meteorol. Soc. 90, 1095–1107.

Hawkins, E., Sutton, R., 2011. The potential to narrow uncertainty in projections of regional precipitation change. Clim. Dyn. 37, 407–418.

Hazeleger, W., Wang, X., Severijns, C., Ştefănescu, S., Bintanja, R., Sterl, A., Wyser, K., Semmler, T., Yang, S., van den Hurk, B., van Noije, T., van der Linden, E., van der Wiel, K., 2012. EC-Earth V2.2: description and validation of a new seamless earth system prediction model. Clim. Dyn. 39, 2611–2629.

IPCC, 2013. Climate Change 2013: The Physical Science Basis. Contribution of Working Group I to the Fifth Assessment Report of the Intergovernmental Panel on Climate Change. In: Stocker, T.F., Qin, D., Plattner, M., Tignor, S.K., Allen, J., Boschung, A., Nauels, Y., Bex, V., Midgley, P.M. (Eds.). Cambridge University Press, Cambridge, United Kingdom and New York, NY, USA, p. 1535.

Ji, D., Wang, L., Feng, J., Wu, Q., Cheng, H., Zhang, Q., Yang, J., Dong, W., Dai, Y., Gong, D., Zhang, R.H., Wang, X., Liu, J., Moore, J.C., Chen, D., Zhou, M., 2014. Description and basic evaluation of beijing normal university earth system model (BNU-ESM) version 1. Geosci. Model Dev. 7, 2039–2064.

Li, Z., Zheng, F., Liu, W., 2012a. Spatiotemporal characteristics of reference evapotranspiration during 1961–2009 and its projected changes during 2011–2099 on the Loess Plateau of China. Agric. For. Meteorol. 154, 147–155.

Li, Z., Zheng, F., Liu, W., Jiang, D., 2012b. Spatially downscaling GCMs outputs to project changes in extreme precipitation and temperature events on the Loess Plateau of China during the 21st Century. Glob. Planet Change 82, 65–73.

Liu, W., Sang, T., 2013. Potential productivity of the Miscanthus energy crop in the Loess Plateau of China under climate change. Environ. Res. Lett. 8, 044003.

Liu, Z., Wang, Y., Shao, M., Jia, X., Li, X., 2016. Spatiotemporal analysis of multiscalar drought characteristics across the Loess Plateau of China. J. Hydrol. 534, 281–299.

Long, M.C., Lindsay, K., Peacock, S., Moore, J.K., Doney, S.C., 2013. Twentieth-century oceanic carbon uptake and storage in CESM1(BGC). J. Clim. 26, 6775–6800.

Marsland, S.J., Bi, D., Uotila, P., Hirst, A.C., 2013. Evaluation of ACCESS climate model ocean diagnostics in CMIP5 simulations. Aust. Meteorol. Oceanogr. 63, 101–119.

Maurer, E.P., Wood, A.W., Adam, J.C., Lettenmaier, D.P., Nijssen, B., 2002. A long-term hydrologically based dataset of land surface fluxes and states for the conterminous United States. J. Clim. 15, 3237–3251.

Meehl, G., Covey, C., Delworth, T., Latif, M., McAvaney, B., Mitchell, J., Stouffer, R., Taylor, K., 2007. The WCRP CMIP3 multi-model dataset: a new era in climate change research. Bull. Am. Meteorol. Soc. 88, 1383–1394.

Miao, C., Ni, J., Borthwick, A.G., Yang, L., 2011. A preliminary estimate of human and natural contributions to the changes in water discharge and sediment load in the Yellow River. Glob. Planet Change 76, 196–205.

Mosier, T.M., Hill, D.F., Sharp, K.V., 2014. 30-Arcsecond monthly climate surfaces with global land coverage. Int. J. Climatol. 34, 2175–2188.

Neale, R.B., Richter, J., Park, S., Lauritzen, P.H., Vavrus, S.J., Rasch, P.J., Zhang, M., 2013. The mean climate of the community atmosphere model (CAM4) in forced SST and fully coupled experiments. J. Clim. 26, 5150–5168.

Ning, L., Bradley, R.S., 2015. Snow occurrence changes over the central and eastern United States under future warming scenarios. Sci. Rep. 5, 17073.

Ning, L., Bradley, R.S., 2016. NAO and PNA influences on winter temperature and precipitation over the eastern United States in CMIP5 GCMs. Clim. Dyn. 46, 1257–1276.

Ning, L., Riddle, E.E., Bradley, R.S., 2015. Projected changes in climate extremes over the northeastern United States. J. Clim. 28, 3289–3310.
Priestley, C., Taylor, R., 1972. On the assessment of surface heat flux and evaporation using large scale parameters. Mon. Weather Rev. 100, 81–92.
Qiao, F., Song, Z., Bao, Y., Song, Y., Shu, Q., Huang, C., Zhao, W., 2013. Development and evaluation of an Earth System Model with surface gravity waves. J. Geophys. Res. 118, 4514–4524.
Ren, H.L., Wu, J., Zhao, C.B., Cheng, Y.J., Liu, X.W., 2016. MJO ensemble prediction in BCC-CSM1.1(m) using different initialization schemes. Atmos. Ocean. Sci. Lett. 9, 60–65.
Rotstayn, L.D., Collier, M.A., Dix, M.R., Feng, Y., Gordon, H.B., O'Farrell, S.P., Smith, I.N., Syktus, J., 2010. Improved simulation of Australian climate and ENSO-related rainfall variability in a global climate model with an interactive aerosol treatment. Int. J. Climatol. 30, 1067–1088.
Schmidt, G.A., Ruedy, R., Hansen, J.E., Aleinov, I., Bell, N., Bauer, M., Bauer, S., Cairns, B., Canuto, V., Cheng, Y., Genio, A.D., Faluvegi, G., Friend, A.D., Hall, T.M., Hu, Y., Kelley, M., Kiang, N.Y., Koch, D., Lacis, A.A., Lerner, J., Lo, K.K., Miller, R.L., Nazarenko, L., Oinas, V., Perlwitz, J., Perlwitz, J., Rind, D., Romanou, A., Russell, G.L., Sato, M., Shindell, D.T., Stone, P.H., Sun, S., Tausnev, N., Thresher, D., Yao, M.-S., 2006. Present-day atmospheric simulations using GISS ModelE: comparison to In situ, satellite, and reanalysis data. J. Clim. 19, 153–192.
Scoccimarro, E., Gualdi, S., Bellucci, A., Sanna, A., Fogli, P.G., Manzini, E., Vichi, M., Oddo, P., Navarra, A., 2011. Effects of tropical cyclones on ocean heat transport in a high-resolution coupled general circulation model. J. Clim. 24, 4368–4384.
Sun, Q., Miao, C., Duan, Q., Wang, Y., 2015. Temperature and precipitation changes over the Loess Plateau between 1961 and 2011, based on high-density gauge observations. Glob. Planet Change 132, 1–10.
Timm, O.E., Giambelluca, T.W., Diaz, H.F., 2015. Statistical downscaling of rainfall changes in Hawai'i based on the CMIP5 global model projections. J. Geophys. Res. 120, 92–112.
Voldoire, A., Sanchez-Gomez, E., Salas y Mélia, D., Decharme, B., Cassou, C., Sénési, S., Valcke, S., Beau, I., Alias, A., Chevallier, M., Déqué, M., Deshayes, J., Douville, H., Fernandez, E., Madec, G., Maisonnave, E., Moine, M.-P., Planton, S., Saint-Martin, D., Szopa, S., Tyteca, S., Alkama, R., Belamari, S., Braun, A., Coquart, L., Chauvin, F., 2013. The CNRM-CM5.1 global climate model: description and basic evaluation. Clim. Dyn. 40, 2091–2121.
Volodin, E.M., Dianskii, N.A., Gusev, A.V., 2010. Simulating present-day climate with the INMCM4.0 coupled model of the atmospheric and oceanic general circulations. Izv. Atmos. Ocean. Phys 46, 414–431.
Wang, L., Chen, W., 2014. A CMIP5 multimodel projection of future temperature, precipitation, and climatological drought in China. Int. J. Climatol. 34, 2059–2078.
Wang, Q., Fan, X., Qin, Z., Wang, M., 2012. Change trends of temperature and precipitation in the Loess Plateau Region of China, 1961–2010. Glob. Planet Change 92, 138–147.
Wang, H.J., Chen, H.P., Liu, J.p., 2015. Arctic sea ice decline intensified haze pollution in eastern China. Atmos. Ocean. Sci. Lett. 8, 1–9.
Watanabe, M., Suzuki, T., O'ishi, R., Komuro, Y., Watanabe, S., Emori, S., Takemura, T., Chikira, M., Ogura, T., Sekiguchi, M., Takata, K., Yamazaki, D., Yokohata, T., Nozawa, T., Hasumi, H., Tatebe, H., Kimoto, M., 2010. Improved climate simulation by MIROC5: mean states, variability, and climate sensitivity. J. Clim. 23, 6312–6335.
Watanabe, S., Hajima, T., Sudo, K., Nagashima, T., Takemura, T., Okajima, H., Nozawa, T., Kawase, H., Abe, M., Yokohata, T., Ise, T., Sato, H., Kato, E., Takata, K., Emori, S., Kawamiya, M., 2011. MIROC-ESM 2010: model description and basic results of CMIP5-20c3 m experiments. Geosci. Model Dev. 4, 845–872.
Willmott, C.J., Matsuura, K., 2005. Advantages of the mean absolute error (MAE) over the root mean square error (RMSE) in assessing average model performance. Clim. Res. 30, 79–82.
Wood, A.W., Maurer, E.P., Kumar, A., Lettenmaier, D.P., 2002. Long-range experimental hydrologic forecasting for the eastern United States. J. Geophys. Res. 107, 4429.
Xin, X.G., Wu, T.W., Li, J.L., Wang, Z.Z., Li, W.P., Wu, F.H., 2013. How well does BCC_CSM1.1 reproduce the 20th century climate change over China? Atmos. Ocean. Sci. Lett. 6, 21–26.
Xu, J., Gao, Y., Chen, D., Xiao, L., Ou, T., 2016. Evaluation of global climate models for downscaling applications centred over the Tibetan Plateau. Int. J. Climatol., http://dx.doi.org/10.1002/joc.4731.
Yukimoto, S., Adachi, Y., Hosaka, M., Sakami, T., Yoshimura, H., Hirabara, M., Tanaka, T.Y., Shindo, E., Tsujino, H., Deushi, M., Mizuta, R., Yabu, S., Obata, A., Nakano, H., Koshiro, T., Ose, T., Kitoh, A., 2012. A new global climate model of the meteorological research institute: MRI-CGCM3 —Model description and basic performance—. J. Meteorol. Soc. Jpn. 90A, 23–64.
Zhang, X., Wang, Q., Mu, M., 2015. The impact of global warming on Kuroshio Extension and its southern recirculation using CMIP5 experiments with a high-resolution climate model MIROC4 h. Theor. Appl. Climatol., http://dx.doi.org/10.1007/s00704-015-1672-y.
Zhao, C., Nan, Z., Feng, Z., 2004. GIS-assisted spatially distributed modeling of the potential evapotranspiration in semi-arid climate of the Chinese Loess Plateau. J. Arid Environ. 58, 387–403.
Zhou, T., Song, F., Chen, X., 2013. Historical evolution of global and regional surface air temperature simulated by FGOALS-s2 and FGOALS-g2: How reliable are the model results? Adv. Atmos. Sci. 30, 638–657.